

WFC3 IR PSF Evaluation in Thermal-Vacuum Test #3

G. F. Hartig
September 16, 2008

ABSTRACT

We have assessed the image quality of the WFC3 IR channel in a flight-like thermal-vacuum environment, and with its flight detector installed. Point source measurements at 16 field positions and three wavelengths indicate good imaging performance for the IR channel. Encircled energies meet expectations over the field, with CASTLE stimulus illumination, when reasonable contributions from detector effects are accounted for. Models including the HST OTA indicate that the on-orbit EE will likely meet all specifications at 1 μ , but that the PSF core EE at 1.6 μ may not reach the spec level, although the specs at larger diameters will readily be met.

Introduction

With the instrument in its final flight configuration we have made new point source image quality measurements with the CASTLE stimulus in the GSFC SES chamber during the thermal-vacuum #3 test (TV3), in Mar-Apr '08. The alignment of the IR detector within WFC3 and of the IR channel with respect to the CASTLE stimulus was determined to be nearly optimal during the TV3 test (Hartig 2008a) and the optical performance over the field, as assessed with wavefront error measurements, is excellent (Hartig 2008b). Here we report the results of encircled energy and azimuthally-averaged PSF intensity measurements over the field. We also present modeling results, including predictions of on-orbit performance, with comparison to the CEI specifications.

Procedure

The PSF data were obtained at three wavelengths and in two epochs, as shown in Table 1. The measurements at 1.06 μ and 1.60 μ were obtained in the “cold operate” environment, while those at 1.31 μ were obtained at “hot operate”. Full frame images were obtained at each of 16 field positions, using the RAPID exposure pattern with 5 or 7 readouts. The CASTLE provided narrow-band point source illumination with laser diode-fed single mode fibers at the two shorter wavelengths; a 10 μ pinhole illuminated via fiber from a tungsten

lamp-fed double monochromator, with 13 nm bandpass, was used for the observations at 1.6 μ . The detector was operated at the nominal –128 C on-orbit temperature.

Table 1. TV3 IR PSF Observation Log

λ (μ)	Filter	SMS	Date	Log	DB ID	Expo
1.06	F105W	IR08S01A	15-Mar-08	2008075a	51814:51834	RAPID/5
1.31	F125W	IR08S02	2-Apr-08	2008093a	55517:55537	RAPID/5
1.60	F160W	IR08S03A	15-Mar-08	2008075a	51793:51813	RAPID/7

In addition to the 16 well-exposed PSF images, several deeper full frame images, with the image cores saturated by factors of ~ 5 and 50, were also obtained at one field point near field center for each of the 3 wavelengths, to better assess the PSF far wings and search for straylight effects. Dark images, following these saturated PSF images, were also obtained to evaluate image persistence effects in the HgCdTe detector; these results are reported elsewhere (STScI ISR WFC3-2008-33, in preparation).

Results

A montage of the images at each field point is displayed for each wavelength, with a log stretch over ~ 6 dex, in Figure 1. The images are magnified by a factor 4 relative to the field size, and are located at the correct relative field positions. The diffraction-induced growth of the PSF with wavelength is readily apparent. The images are well centered with respect to the format and no rotation is apparent, indicating excellent detector alignment. Several of the images unfortunately lie directly upon bad detector pixels; their EE values are shown as 0, since accurate measurement is not possible.

The raw IR images are first processed to correct for nonlinearity, subtract a “super-dark” reference image, compute the count rate for each pixel from the multi-accum mode ramp, rejecting saturated readouts, and apply a flat field correction. The encircled energy (EE) as function of radius from PSF center was then computed for each of the images, using IDL code previously developed and used for COSTAR, STIS and ACS alignment and verification. Briefly, the code corrects for first-order geometrical distortion, finds the image center at which the EE in a small diameter (0.25 arcsec) is maximized, computes the radius of each pixel from that center and, after subtracting a background that is adjusted so that the EE curve asymptotes to 1 with 0 gradient at a specified radius, sums the normalized flux contribution within discrete radii, including estimation of partial pixel contributions. Table 2 presents the EE, in diameters of 0.25, 0.37 and 0.60 arcsec, averaged over the field; the results for each of the measured field points are presented in Table 3, and shown in Figure 1 for diameters listed in the caption. The peak pixel fraction (useful for exposure time estimation with regard to saturation avoidance), image width in pixels and sharpness parameter (sum of square of unity-sum-normalized PSF) are also included in Tables 2 and 3. Note that the peak fraction is highly sensitive to centration on the pixel grid, especially in the case here where the Airy disk is undersampled. Modeling has shown that PSFs centered on the pixel corners can produce peak fraction $\sim 60\%$ lower than those centered on a pixel, at 1 μ .

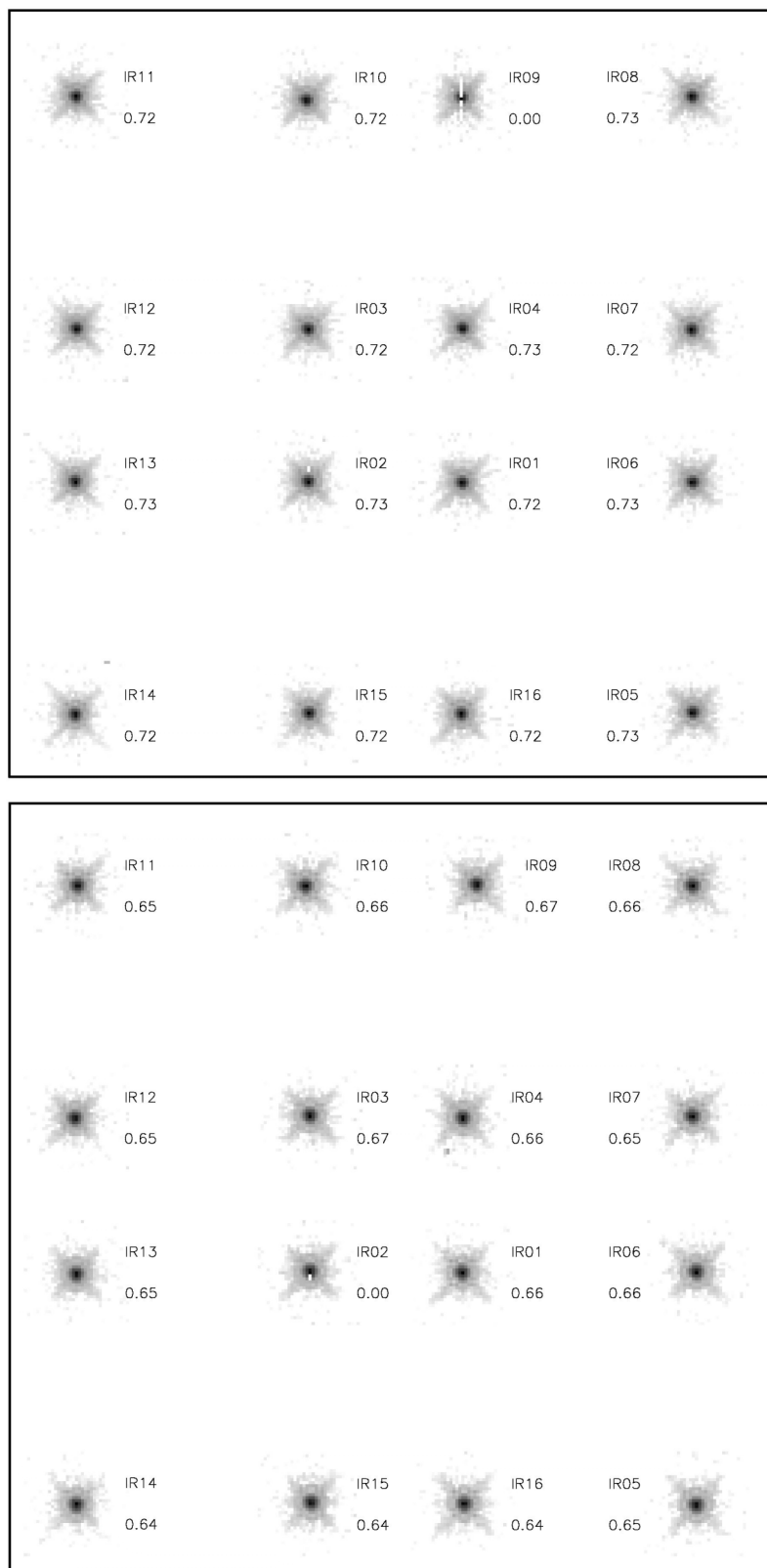


Figure 1. Montages of measured PSF images at 16 field points and at wavelengths 1.06μ (top) and 1.31μ (bottom). The images, shown centered at their actual locations in the field of view but with magnification of 4, have had background subtracted and first-order geometrical distortion removed. Measured encircled energies within a 0.37 arcsec diameter are shown.

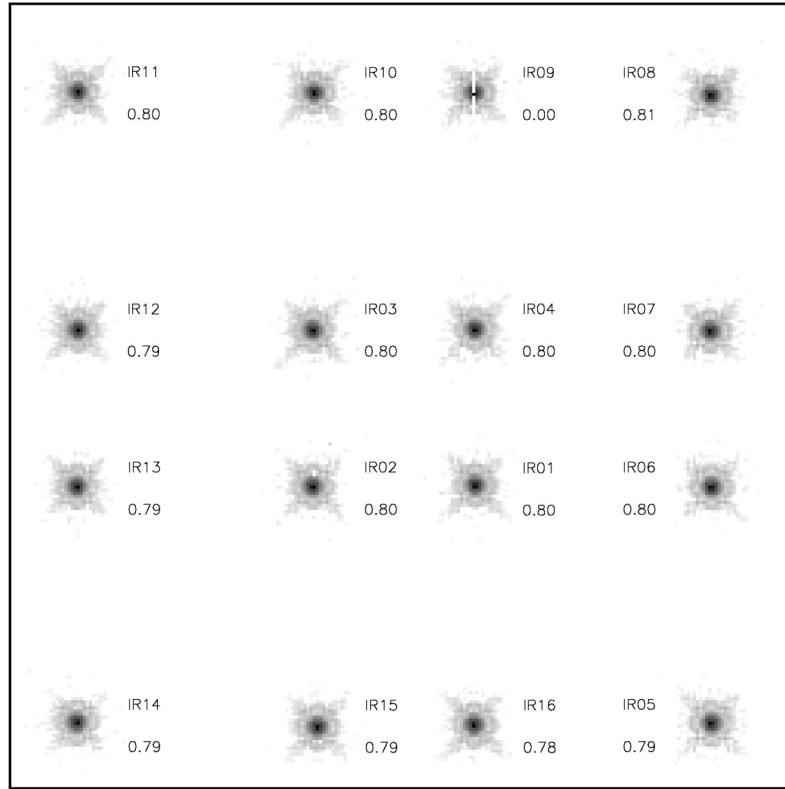


Figure 1 (cont'd). Montages of measured PSF images at 16 field points at wavelength 1.06μ indicating encircled energies within 0.60 arcsec diameter.

Table 2. Mean Measured Encircled Energy and Other PSF Parameters

IR PSF Parameter Average Over Field						
λ (μ)	peak	EE(0.25)	EE(0.37)	EE(0.6)	FWHM	sharp
1.06	0.260	0.520	0.723	0.865	1.417	0.116
1.31	0.223	0.462	0.653	0.841	1.517	0.095
1.60	0.209	0.415	0.578	0.796	1.466	0.080

For a more extensive assessment of the PSF at several points near field center, long-exposure, saturated images were obtained and with the (non-destructive read multi-accum mode) STEP-400 pattern. The count rate for each pixel was determined using only non-saturated samples after rudimentary correction for non-linearity, producing the high dynamic range images shown in Figure 2, with a log stretch from 0.005 to 5000 e^-/s . The images subtend 16 arcsec square. The growth of the Airy rings with wavelength is apparent, as is the $\sim 10\%$ anamorphic distortion (vertical elongation) due predominantly to the focal plane tilt. Some residual warm and dead pixels may also be seen; two of the latter unfortunately occur near the core of the PSF at 1.31 μ , rendering accurate evaluation of EE, etc., impossible for that image. The spider diffraction is also somewhat unusual, as it results from the interplay of the wider cold mask spiders in WFC3 with the spider in the CASTLE stimulus, which rotate somewhat relative to the former, depending on field position. In the HST, the cold mask spiders are expected to completely mask those of the OTA. Likewise, the cold mask central obscuration is designed to mask that of the OTA SM, but the CASTLE obscuration is larger and extends beyond the cold mask, resulting in

more PSF energy redistribution from the Airy disk into the rings than will be seen on-orbit. No imaging or straylight artifacts are apparent in these images.

Table 3. Measured Encircled Energies and other parameters

IR01						
λ (μ)	peak	0.25	0.37	0.6	FWHM	sharp
1.06	0.244	0.510	0.721	0.867	1.502	0.108
1.31	0.291	0.490	0.655	0.842	1.250	0.113
1.60	0.144	0.391	0.590	0.798	1.840	0.069
IR02						
λ (μ)	peak	0.25	0.37	0.6	FWHM	sharp
1.06	0.311	0.536	0.727	0.861	1.234	0.131
1.31	0.000	0.000	0.000	0.000	0.000	0.000
1.60	0.207	0.412	0.570	0.798	1.465	0.079
IR03						
λ (μ)	peak	0.25	0.37	0.6	FWHM	sharp
1.06	0.334	0.555	0.723	0.868	1.208	0.141
1.31	0.264	0.483	0.665	0.845	1.363	0.106
1.60	0.212	0.413	0.579	0.799	1.461	0.079
IR04						
λ (μ)	peak	0.25	0.37	0.6	FWHM	sharp
1.06	0.191	0.497	0.726	0.864	1.595	0.101
1.31	0.212	0.474	0.658	0.842	1.528	0.096
1.60	0.203	0.411	0.581	0.801	1.479	0.078
IR05						
λ (μ)	peak	0.25	0.37	0.6	FWHM	sharp
1.06	0.239	0.510	0.728	0.865	1.476	0.108
1.31	0.187	0.450	0.647	0.843	1.641	0.087
1.60	0.199	0.402	0.564	0.790	1.484	0.074
IR06						
λ (μ)	peak	0.25	0.37	0.6	FWHM	sharp
1.06	0.250	0.526	0.728	0.866	1.444	0.114
1.31	0.277	0.480	0.656	0.842	1.292	0.108
1.60	0.174	0.401	0.581	0.802	1.671	0.073
IR07						
λ (μ)	peak	0.25	0.37	0.6	FWHM	sharp
1.06	0.286	0.528	0.719	0.864	1.355	0.120
1.31	0.240	0.468	0.649	0.834	1.419	0.096
1.60	0.213	0.424	0.583	0.798	1.436	0.082
IR08						
λ (μ)	peak	0.25	0.37	0.6	FWHM	sharp
1.06	0.233	0.510	0.733	0.871	1.523	0.107
1.31	0.271	0.484	0.664	0.844	1.324	0.107
1.60	0.169	0.404	0.599	0.811	1.749	0.073
IR09						
λ (μ)	peak	0.25	0.37	0.6	FWHM	sharp
1.06	0.000	0.000	0.000	0.000	0.000	0.000
1.31	0.180	0.444	0.666	0.849	1.730	0.085
1.60	0.000	0.000	0.000	0.000	0.000	0.000
IR10						
λ (μ)	peak	0.25	0.37	0.6	FWHM	sharp
1.06	0.182	0.489	0.723	0.864	1.654	0.099
1.31	0.226	0.471	0.659	0.838	1.495	0.096
1.60	0.214	0.432	0.591	0.804	1.441	0.084
IR11						
λ (μ)	peak	0.25	0.37	0.6	FWHM	sharp
1.06	0.274	0.522	0.720	0.859	1.378	0.116
1.31	0.186	0.450	0.649	0.833	1.626	0.085
1.60	0.252	0.438	0.583	0.799	1.285	0.091
IR12						
λ (μ)	peak	0.25	0.37	0.6	FWHM	sharp
1.06	0.239	0.509	0.724	0.863	1.494	0.107
1.31	0.162	0.430	0.653	0.842	1.801	0.080
1.60	0.261	0.434	0.569	0.790	1.243	0.091
IR13						
λ (μ)	peak	0.25	0.37	0.6	FWHM	sharp
1.06	0.311	0.536	0.726	0.865	1.240	0.131
1.31	0.210	0.465	0.651	0.842	1.554	0.093
1.60	0.237	0.420	0.568	0.790	1.298	0.083
IR14						
λ (μ)	peak	0.25	0.37	0.6	FWHM	sharp
1.06	0.213	0.509	0.716	0.868	1.526	0.107
1.31	0.253	0.461	0.642	0.843	1.394	0.097
1.60	0.215	0.406	0.571	0.786	1.378	0.077
IR15						
λ (μ)	peak	0.25	0.37	0.6	FWHM	sharp
1.06	0.322	0.544	0.720	0.871	1.243	0.135
1.31	0.174	0.423	0.639	0.835	1.797	0.078
1.60	0.215	0.420	0.571	0.787	1.403	0.082
IR16						
λ (μ)	peak	0.25	0.37	0.6	FWHM	sharp
1.06	0.271	0.525	0.716	0.864	1.382	0.118
1.31	0.212	0.457	0.641	0.839	1.538	0.092
1.60	0.221	0.418	0.569	0.783	1.355	0.081

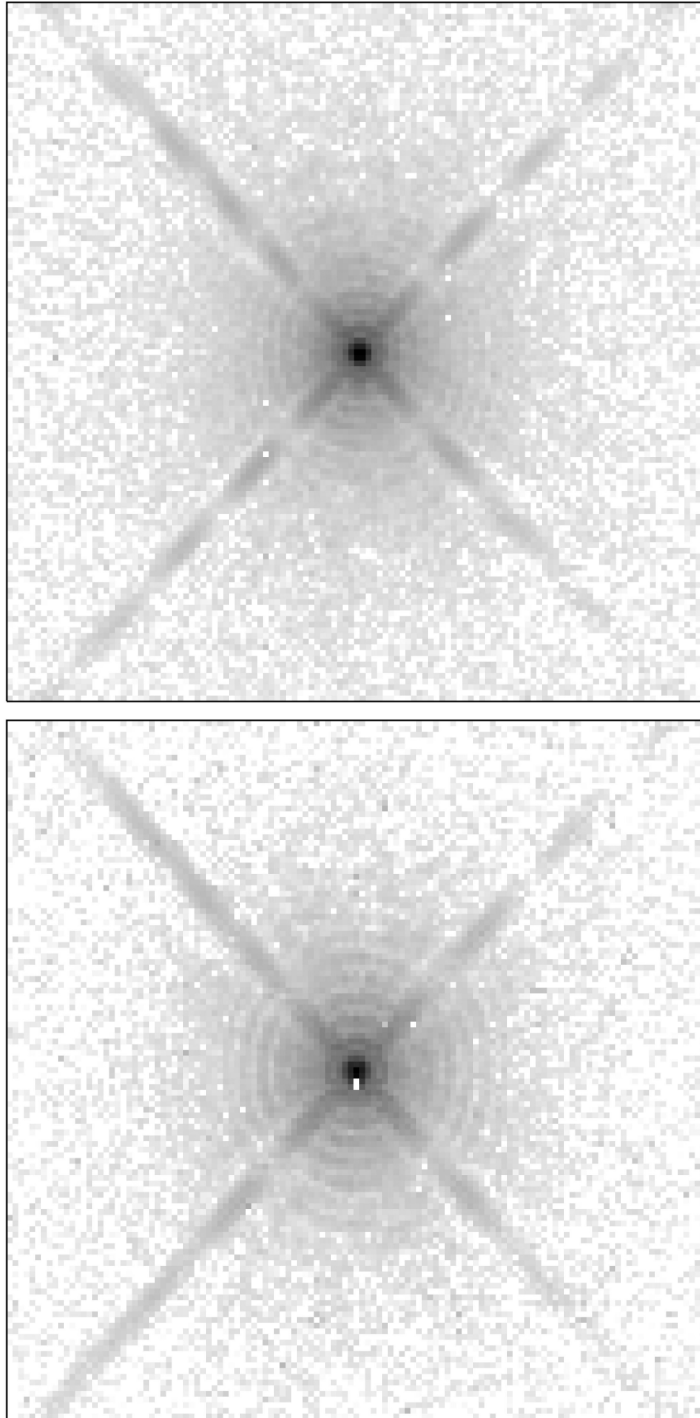


Figure 2. High dynamic range composite images at 1.06μ (top, at IR01) and 1.31μ (bottom, at IR02) shown on a 6 dex log stretch, covering 16 arcsec square.

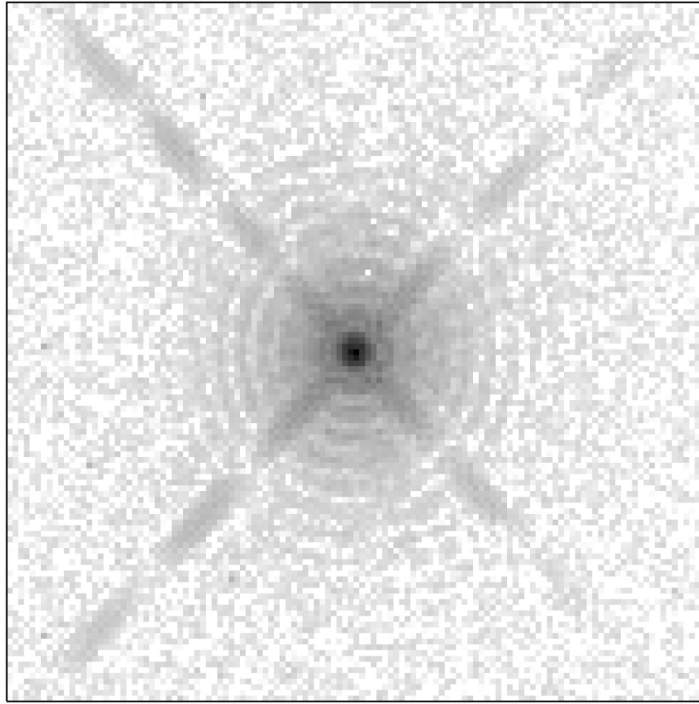


Figure 2 (cont'd). High dynamic range composite images at 1.6 μ (at IR03) shown on a 6 dex log stretch, covering 16 arcsec square.

In order to extrapolate these lab data to expected on-orbit results, we begin with modeling the images using straightforward calculations, including only an independent assessment of the low order WFE (Hartig, 2008b), the CASTLE pupil mask and a reasonable estimate of the detector MTF, due to inter-pixel capacitance and charge diffusion. The latter are approximated by convolving the PSF with a Gaussian jitter kernel, and may be anchored with an early DCL measurement of the HgCdTe detector pixel response function (PRF) (Russell, private communication, 2004).

We may attempt to independently estimate the PRF by comparing model PSFs with the observed images at each wavelength. The peak fraction is quite sensitive to the PRF, but, unfortunately, it is also very sensitive to image centration with respect to the pixel boundaries. The EE, even in a relatively small diameter (0.25 arcsec) is relatively insensitive to both charge diffusion and PSF centration. The image width, as assessed by a subsampling Gaussian fit algorithm, and the PSF sharpness are better parameters for this fit, as they are relatively insensitive to centration while retaining significant sensitivity to the PRF. The adopted modeling approach matches the distribution of the ensemble of these parameters with the measured results shown in Tables 2 and 3, by applying varying amounts of “jitter” and offsets from pixel center. The best empirical fit to the pixel response convolution kernel is shown in Table 4, approximated as 34 mas RMS Gaussian jitter. This is a reasonable match to the DCL measurement, which showed 91% in the central pixel (for an unthinned, non-flight detector at 1.31 μ). These results indicate that the CEI specification requiring that 90% of the energy from a small spot lie within the central pixel is just met.

Table 4. IR-4 Detector Pixel Response Function Kernel

IR-4: All wavelengths		
0.0007	0.025	0.0007
0.025	0.897	0.025
0.0007	0.025	0.0007

For the high SNR images at 1.06 and 1.60 μ shown in Fig 2 we have computed the EE and azimuthally-averaged (AA) PSF, normalized to 1 at the peak, for comparison with the CASTLE+WFC3 model. These are shown in Figure 3, which plots the measured EE (left panel) and AA PSF intensity (right panel) as solid lines, with the CASTLE+WFC3 model shown as dotted lines. The agreement between measurement and model is very good, from radii of 130 mas (1 px) to 5 arcsec. The differences in modulation of the AA PSF wings beyond 1 arcsec are at least partially due to inaccuracies in the model related to the diffraction of the spiders.

Because the EE specification applies to the WFC3 installed in the HST, the ground-based measurements must be extrapolated with the aid of model computations that account for differences between the CASTLE and HST to predict on-orbit performance. These differences include the smaller central obscuration of the OTA, its PM mounting pads, and the mid-spatial-frequency zonal polishing errors of its mirrors. The EE specifications in the PSF wings (for 1.0 and 1.6 μ) are shown in Figure 3 as diamonds. On-orbit performance, including the HST telescope properties, is approximated by the dashed OTA+WFC3 model curves.

While the projected on-orbit PSF core EE (dashed line) at 1.06 μ , (53% in 0.25 arcsec diameter) falls shy of the 1.00 μ specification (56%) shown, our model shows that the improvement in performance accruing from shrinkage of the Airy disk from 1.06 to 1.00 μ brings the core EE just into spec. At larger diameters, the on-orbit EE performance should readily meet spec at all wavelengths. At 1.6 μ , however, the difficult core EE spec (48% within 0.25 arcsec diameter) will not likely be met on-orbit, as shown in the figure. This is due to the increased role of detector-induced blur as the Airy disk expands, pushing more energy over the EE diameter boundary into neighboring pixels. The spec level is ill-conceived, since the model, which includes only the measured WFE (which is well in spec), the detector blur (just in spec), the instrument pupil geometry, and known properties of the OTA, predicts a lower value (46%). As noted above, all of the PSF performance parameters are sensitive to centration on the detector pixel array and limitations in our ability to assess their true values given the pixelation of the highly undersampled images produced by the WFC3 IR channel.

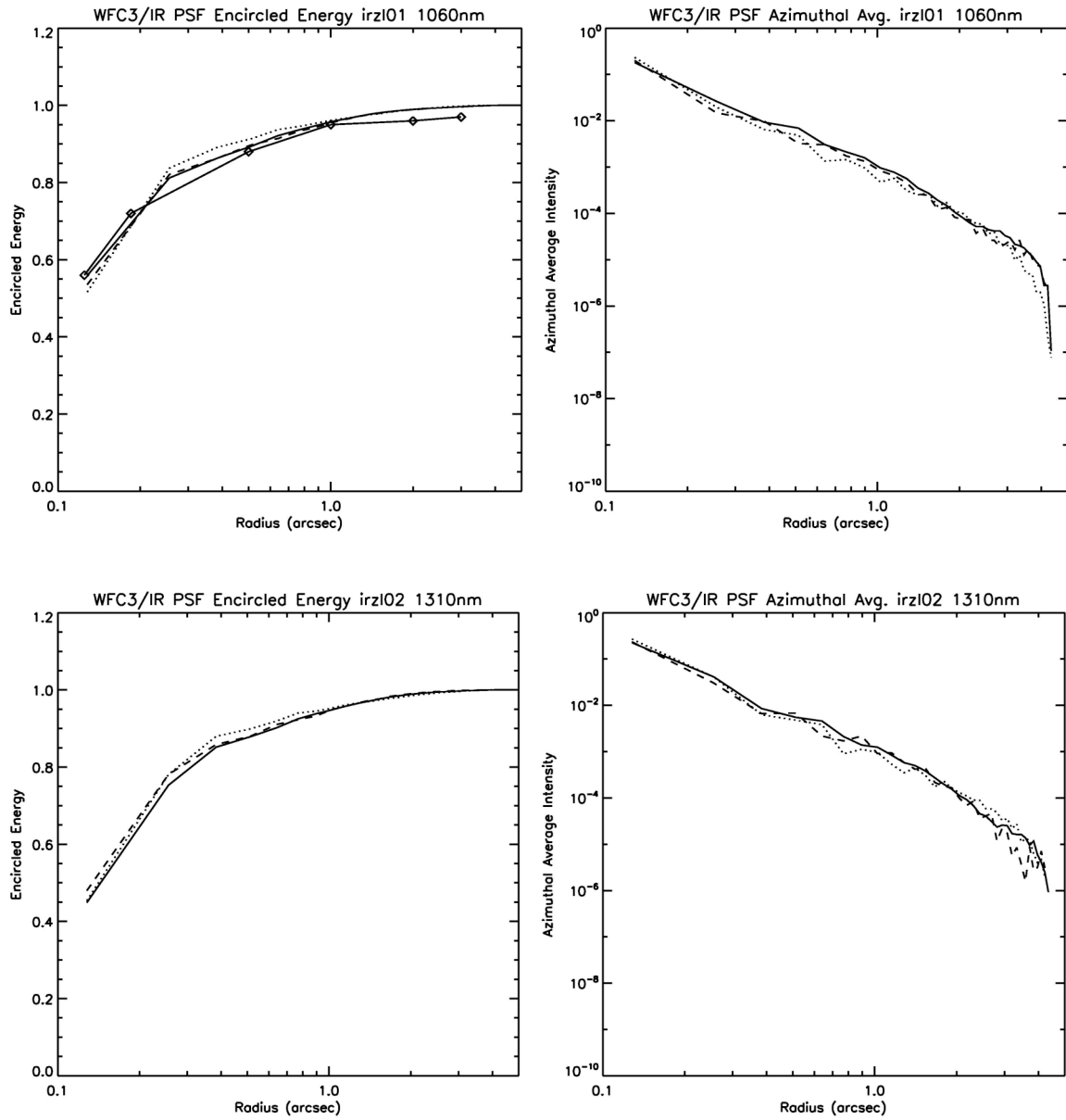


Figure 3. Comparison of composite measured (solid line), CASTLE model (dotted line), and OTA model (dashed line) images at field points IR01 and IR02 at 1.06, and 1.31 μm , respectively. The left frames show the encircled energy, from radii of 1 px to 5 arcsec, and the right frames plot the azimuthally-averaged PSF. The EE specifications (at 1.0 μm) are shown as diamonds.

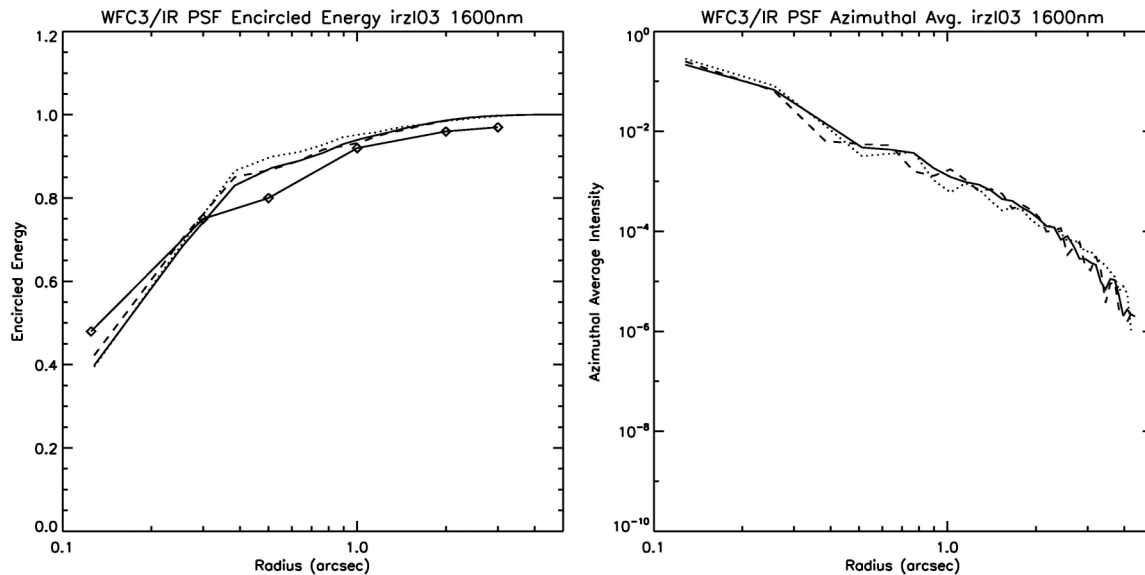


Figure 3 (cont'd.) Comparison of composite measured (solid line), CASTLE model (dotted line), and OTA model (dashed line) images at field point IR03 at 1.60 μ . The left frame shows the encircled energy, from radii of 1 px to 5 arcsec, and the right frame plots the azimuthally-averaged PSF. The EE specifications are shown as diamonds.

Conclusion

We conclude that the flight configuration WFC3 IR channel optical performance is generally excellent and performs as expected over the field. Our modeling indicates that the IR channel will meet all of its on-orbit image quality (EE) specifications at 1.0 μ ; the core PSF requirement at 1.6 μ will likely be approached, but not achieved, due to detector effects on the highly undersampled images.

References

Hartig, G.F., "WFC3 Optical Alignment Characterization in Thermal-Vacuum Test #3", WFC3 ISR 2008-32 (2008a).

Hartig, G.F., "WFC3 Optical Wavefront Error Characterization in Thermal-Vacuum Test #3", WFC3 ISR 2008-31 (2008b).